Effect of uniaxial stress on the polarization of light emitted from GaN/AlN quantum dots grown on Si(111)

O. Moshe and D. H. Rich
Department of Physics, The Ilse Katz Center for Nano and Meso Scale Science and Technology, Ben-Gurion University of the Negev, P.O. Box 653, Beer-Sheva 84105, Israel

B. Damilano and J. Massies
Centre de Recherché sur l'Hetero-Epitaxie et ses Applications, Centre National de la Recherche, Rue B. Gregory, Sophia Antipolis, 06560 Valbonne, France

(Received 26 November 2007; revised manuscript received 22 January 2008; published 23 April 2008)

Cathodoluminescence (CL) measurements of the ground-state excitonic transition of vertically stacked GaN/AlN quantum dots (QDs) exhibited an in-plane linear polarization anisotropy in close proximity to microcracks. Microcracks form as a result of a mismatch of the thermal expansion coefficient between the GaN/AlN layers and the Si(111) substrate. In close proximity to the cracks, the layers are found to be under uniaxial tensile stress, whereas the film is under biaxial tensile stress for distances greater than ~ 3 μm from the cracks. The microcracks serve as an excellent stressor through which the strain tensor of the GaN/AlN QDs can be reproducibly modified for studies of strain-induced changes in the optical and electronic properties by using a spatially resolved probe, such as with CL. Changes in the optical properties of the QDs are attributed to stress-dependent variations of the band edges and the electric field along [0001], which is caused by charge polarization. Such changes in the field will subsequently affect the oscillator strength between electrons and holes. Three-dimensional 6×6 $\boldsymbol{k}\cdot\boldsymbol{p}$ calculations of the QD electron and hole wave functions and eigenstates were performed to examine the influence of biaxial and uniaxial tensile stresses on the polarization-dependent momentum matrix element in varying proximity to the microcracks. The model reveals that a change from biaxial to uniaxial stress alters the admixture of p_x and p_y characters of the band edges and the ground-state hole wave function, changes the shape and direction of elongation of the hole isosurfaces, and accounts well for the subsequent anisotropy in the polarization dependent optical transitions.

DOI: 10.1103/PhysRevB.77.155322 PACS number(s): 78.67.−n, 78.66.−w, 78.60.Hk

I. INTRODUCTION

Self-assembled quantum dots (QDs) that are composed of group III-nitride materials have attracted much interest in recent years. The high luminescence efficiency in the visible to ultraviolet spectral range of these QDs shows great promise for the fabrication of variable wavelength lasers and light emitting diodes.[1–3] An important issue that remains a topic of interest in this system is the excitation dependence of the electric field in the QD, which originates from piezoelectric and pyroelectric charge polarizations. The field is the source of a quantum-confined Stark effect (QCSE) that induces a strong redshift in the excitonic luminescence spectra and lowers the QD excitonic transition energy to a value that is well below the GaN bulk transition energy.[2–5] The field is estimated to be $\sim 5-7$ MV/cm and is mainly oriented along the [0001] direction.[5,6] A field as large as 9 MV/cm was recently reported for a single layer of GaN QDs grown on either *c*-plane sapphire or Si(111) substrates.[7] A second issue is the choice of suitable substrates on which to grow group III-nitride heterostructures.[8] Si is a common substrate that exhibits a large mismatch in thermal expansion coefficient with group III-nitride films, and heteroepitaxy can lead to the formation of microcracks in the film during the postgrowth cooling of the wafer. A more rapid contraction of the film leads to a large tensile stress in the grown material, which is then relieved by the formation of cracks.[9] Another important feature of the microcracks is that they locally perturb the QD strain tensor, thereby enabling a study of strain-induced changes in the electronic structure and subsequent effects on the QD optical properties. Thus, the microcracks can serve as an excellent stressor through which the strain tensor of the GaN/AlN QDs can be reproducibly modified for studies of strain-induced changes in the optical and electronic properties by using a spatially resolved optical probe, such as cathodoluminescence (CL) imaging and spectroscopy.

A previous study of similar microcracks used CL wavelength imaging and micro-Raman spectroscopy to examine $Al_{0.17}Ga_{0.83}N/GaN$ thin films grown on a thermally mismatched (0001) sapphire substrate.[10] The results showed that in regions far from the microcracks (greater than ~ 3 μm), the stress tensor in the layer has a biaxial form such that $\sigma_{xx}=\sigma_{yy}$ and in close proximity to the microcrack, the stress has a uniaxial form, in which $\sigma_{xx}=0$ and $\sigma_{yy}>0$.[10] We define the x and y coordinates to represent directions perpendicular and parallel to the microcracks, respectively, and this convention will be used throughout this paper. In a recent study of GaN/AlN QDs grown on Si, we demonstrated that a local modification of the strain tensor can be probed with time-resolved CL, which revealed changes in the exciton lifetime in close proximity to microcracks that correlated with calculated changes in the exciton oscillator strength.[11]

Extensive data exist on the optical polarization anisotropy for group III-nitride semiconductors films and light emitting devices.[12,13] Such an anisotropy was detected between the σ-polarized mode ($\boldsymbol{E}\perp\boldsymbol{c}$) and the π-polarized mode ($\boldsymbol{E}\parallel\boldsymbol{c}$),

where $\boldsymbol{c}$ represents the $\boldsymbol{c}$-axis translation vector of the wurtzite structure along [0001].[14] The σ and π polarization modes originate from the orthogonal p-orbital characters of the heavy-hole (hh) and crystal-field split-off-hole valence bands for III-nitride semiconductors with a wurtzite structure.[14,15] As for an in-plane polarization anisotropy of the σ-polarized mode ($\boldsymbol{E}\perp\boldsymbol{c}$) in quantum wells and QDs grown in the $\boldsymbol{c}$-plane (0001) orientation, in which light emission or absorption depends on the orientation of $\boldsymbol{E}$ relative to the $[1-100]$ or $[11-20]$ directions, fewer results appear in the literature. Rau *et al.*[16] showed that quantum confinement in $GaN/Al_{0.1}Ga_{0.9}N$ multiple quantum wells grown on the $\boldsymbol{m}$-plane $(1-100)$ exhibits an in-plane polarization anisotropy that was attributed to a confinement-induced admixture of p_z orbitals in the ground-state hh excitonic transition. More recently, an in-plane anisotropy in narrow polarized emission lines from excitonic complexes in single InGaN/GaN QDs has recently been reported and was attributed to the different hole characters present in excitons that are derived from the top two valence bands.[17]

In this paper, we present results showing that an optical polarization anisotropy in QDs can be induced by an external stressor in the form of microcracks. It is normally difficult to locally perturb the strain tensor of QDs in a reliable and reproducible way, and microcracks present a scheme for such a perturbation. We present results of linearly polarized CL measurements of vertically stacked GaN/AlN QDs grown on Si(111) in varying proximity to microcracks. We show that the polarization anisotropy in QD emission occurs within a length scale of a few micrometers from a microcrack, where the stress tensor of the film exhibits a form that is approximately uniaxial. In regions far from the crack where the stress tensor is nearly biaxial, an anisotropy in polarization is not detected. We examined the spatial dependence of this anisotropy in detail. We also present a theoretical model to explain the dependence of the anisotropy as a function of distance from a microcrack. Three-dimensional (3D) calculations of the QD electronic states by using an effective mass method for electrons and a 6×6 $\boldsymbol{k}\cdot\boldsymbol{p}$ method for holes were performed to examine the influence of biaxial and uniaxial tensile stresses on the polarization-dependent momentum matrix element in varying proximity to the microcracks. The model utilizes various parameters, including the strain tensor, spin-orbit coupling, and spontaneous and piezoelectric charges. A comparison to the experimental results is presented in an attempt to understand the cause of the in-plane polarization anisotropy.

II. EXPERIMENTAL METHOD AND SETUP

The samples were grown by molecular beam epitaxy by using the two-dimensional to 3D Stranski–Krastanov Growth mode transition.[18,19] Two samples were grown on Si (111) substrates and consist of AlN (30 nm)/GaN (400 nm)/AlN (700 nm) buffer layers followed by either 40 or 85 layers of GaN QDs, which where labeled as samples S-40 and S-85, respectively. The growth of sample S-40 (S-85) involved 18-nm-(6.7-nm-) thick AlN barrier layers with 2.6-nm-(1.6-nm-) thick GaN dot layers, resulting in an average dot height of ~5 nm (~3.7 nm), as previously determined by transmission electron microscopy (TEM) measurements for samples possessing very similar structures and growth conditions.[5] Both samples were terminated with a 40-nm-thick AlN capping layer. The average dot density is $\sim5\times10^{11}$ cm^{-2}.[5]

The linearly polarized cathodoluminescence detection system is installed on a JEOL 5910 scanning electron microscope (SEM) with modified ports for an optical system to collect luminescence from samples mounted on a variable temperature stage. The stage is connected via a copper braid to a closed-cycle He cryorefrigerator. An ellipsoidal mirror with variable three-axis positioning collects luminescence emitted from the sample. The emitted luminescence is collected by the mirror and focused onto a coherent optical fiber bundle with a vacuum rotatable linear polarizer positioned before the fiber optics.[20] Two polarization directions for the polarizer will be denoted with the subscripts $\perp$ and $\parallel$ to indicate detection orientations with $\boldsymbol{E}$ perpendicular and parallel to a microcrack that is oriented along the $[11-20]$ crystallographic direction.[20] The polarization anisotropy ratio R_p is defined by the ratio of CL intensities I under the two orthogonal polarizer orientations and is given by $R_p=I_\perp/I_\parallel$. In order to account for polarization mixing caused by reflection at the mirror, e.g., due to the finite solid angle of collection, a linearly polarized Lambertian (cosine) source was placed at the focus to simulate emission from the sample. The minimum value of R_p, which was obtained by rotating the detection polarizer 90° relative to the source polarization, deviated from the ideal value of 0 and was found to be $R_{p(\min)}\approx0.27$. Likewise, a maximum value for R_p was determined by rotating the polarized source 90° and yielded $R_{p(\max)}\approx1/R_{p(\min)}\approx3.7$. The light from the flexible fiber bundle was transferred to a 1/4 m monochromator outside the SEM vacuum system. The spectral resolution of the monochromator was 2 nm (~15 meV) at $\lambda=400$ nm (3.10 eV). The dispersed light was detected with a multialkali photomultiplier tube, which enabled photon counting.

The intensities $I_\perp$ and $I_\parallel$ were examined with the acquisition of monochromatic CL images and position-dependent local spectra, in which the e-beam was fixed at a spot during the measurement of a CL spectrum. From the CL images, a pixel analysis was performed so as to generate a line-scan profile showing $I_\perp$ or $I_\parallel$ vs distance from the microcrack. CL images were acquired by scanning over a 12.8×9.6 μm^2 size region surrounding the microcracks. CL images and spectra were acquired while the samples were maintained at temperatures of ~300 or 91 K. A beam current of $I_b=200$ pA with a beam energy of $E_b=15$ keV was used to probe the sample. The effective spatial resolution for these imaging conditions is ~0.3 μm for the present samples. A further reduction of the beam current did not appreciably alter the energy position, the line shape, the spectral width, or the polarization anisotropy of the CL spectra, suggesting that we sufficiently employed low excitation conditions so as to minimize the effects of state filling by excited carriers and internal screening of the electric field.

III. THEORETICAL CALCULATIONS USING A THREE-DIMENSIONAL $k \cdot p$ METHOD

The electron and hole wave functions and eigenstates were obtained with 3D 6×6 $\boldsymbol{k} \cdot \boldsymbol{p}$ calculations by using the NEXTNANO[3] quantum nanostructure simulation code.[11,21] The calculations utilized a 3D Schrödinger equation for wurtzite materials, including strain, deformation potentials, spin-orbit coupling, and piezoelectric and pyroelectric charges, the latter of which accounts for the large polarization field in the QD along the [0001] growth direction. In order to calculate the wave functions, a single band model for the electrons and a six-band $\boldsymbol{k} \cdot \boldsymbol{p}$ Hamiltonian for the holes were employed. The coupling between the conduction and valence bands was neglected, owing to the size of the GaN and AlN band gaps.[22]

The choice of the pyroelectric (spontaneous polarization) constants P_{sp} will have an appreciable effect on the resulting electric field in the QD. We employed the material parameters previously used for calculations of the polarization field and eigenstates in GaN/AlN QDs.[23–25] The fully strained GaN/AlN QDs were simulated by minimization of the elastic energy within a continuum model approach that takes into account the symmetry of the hexagonal crystal structure. We employed a simulated region size of $19 \times 19 \times 22$ nm^3 containing a single pyramidal QD with a typical discretized grid of $56 \times 68 \times 80$ nodes for calculations of the strain minimization, Pikus–Bir, $\boldsymbol{k} \cdot \boldsymbol{p}$, and single band effective mass Hamiltonians. External tensile stresses ranging from purely biaxial to uniaxial were used to simulate the thermal stress in varying proximity to the microcracks. We did not consider the effects of Coulomb fields because, as mentioned in Sec. II, the electron-hole excitation density and state filling effects are evidently small. Moreover, the *e-h* Coulomb interaction would only slightly contribute to the transition energies (i.e., we estimate a contribution that is less than ~50 meV, depending on the QD height).[22,26]

IV. EXPERIMENTAL RESULTS AND DISCUSSION

A plan-view SEM image showing a single microcrack running along the [11−20] direction in sample S85 is shown in Fig. 1(a). Local CL spectra were acquired along the direction of the white-dashed line in Fig. 1 (the [1−100] direction) as a function of distance Δx from the microcrack and shown as stack plots in Fig. 2 for both samples S40 and S85. During the measurements, the polarizer was set to detect emission with $\boldsymbol{E} \| [11-20]$ and $\boldsymbol{E} \perp [11-20]$, which are labeled as $\boldsymbol{E}_{\|}$ and $\boldsymbol{E}_{\perp}$, respectively, in Fig. 2. The excitonic peak energy positions E_x for both samples are approximately independent of the e-beam position relative to the cracks. A reduced tensile strain near the microcracks (i.e., $\sigma_{xx} \approx 0$) will tend to increase the piezoelectric contribution to the field and lower E_x as a result of the QCSE. However, this is nearly evenly balanced by an increase in the effective band gap caused by an increased compressive stress on the QDs near the microcracks.[11] These two equal yet opposing effects, namely, a field-induced energy change (redshift) and a compressive strain-induced energy change (blueshift) in the gap, must move in opposite directions as the e-beam is progressively positioned closer to a microcrack to account for a nearly constant excitonic transition energy. Also in Fig. 2, we show values for the anisotropy ratio for polarization, $R_p = I_{\perp}/I_{\|}$, for each set of polarized spectra. The integrated intensity $I_{\perp,\|}$ for each spectrum was used to determine R_p. The largest ratio, $R_p \approx 1.44$, is observed for the spectrum in close proximity to a microcrack, whereas the ratio approaches unity for distances greater than ~3 μm from the crack. The CL intensity is reduced when the e-beam is directly positioned at the edge of the crack as a result of a partial scattering of high-energy electrons into the crack region.

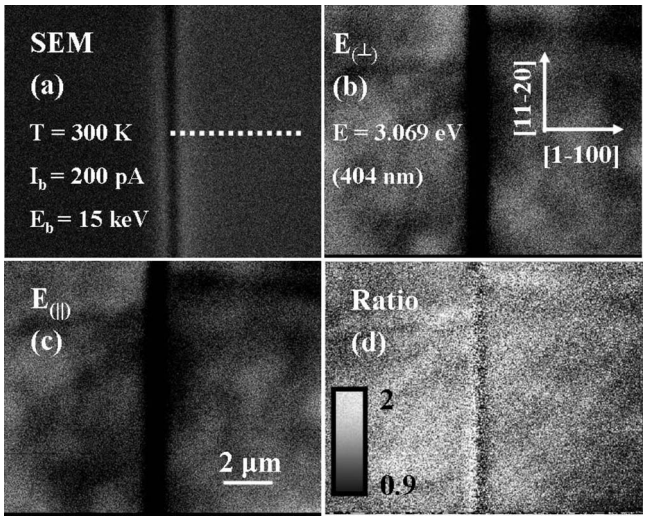

FIG. 1. SEM image of a microcrack in (a), monochromatic CL images with polarization detection conditions of $\boldsymbol{E} \perp [11-20]$ and $\boldsymbol{E} \| [11-20]$ in (b) and (c), respectively, and an image of the anisotropy ratio, $I_{\perp}(x,y)/I_{\|}(x,y)$, in (d) for sample S85. The CL images were acquired with $\lambda = 404$ nm ($h\nu = 3.069$ eV), $T = 300$ K, $I_b = 200$ pA, and $E_b = 15$ keV. The effective spatial resolution for these imaging conditions and current samples is ~0.3 μm.

In order to analyze more carefully the spatial distribution of polarized emission near the microcracks, we performed a series of CL monochromatic images at $\lambda = 404$ nm (3.07 eV) for sample S85 and $\lambda = 476$ nm (2.60 eV) for sample S40, with the polarizer oriented to detect emission with $\boldsymbol{E} \| [11-20]$ and $\boldsymbol{E} \perp [11-20]$. Figure 1 shows one set of these images for sample S85. When the polarizer is oriented to detect emission with the $\boldsymbol{E}_{\perp}$ orientation in Fig. 1(b), the average CL intensity for regions having distances less than ~3 μm from the crack is larger than that for detection with the $\boldsymbol{E}_{\|}$ orientation, as shown in Fig. 1(c). The anisotropy ratio, $R_p = I_{\perp}(x,y)/I_{\|}(x,y)$, which is a pixel-by-pixel ratio of the images of Figs. 1(b) and 1(c) is shown in Fig. 1(d). In most regions near the crack, the ratio is greater than 1, indicating a polarization anisotropy. There are some regions far from the crack in Fig. 1(d) that also exhibit an intensity ratio that deviates from unity. This can be explained by the presence of threading dislocations with their characteristic strain fields, inhomogeneities during growth that can lead to an anisotropic thermal strain upon cooling, and the presence of smaller cracks with narrow gaps which are more difficult to detect with SEM imaging.

A line-scan analysis of the polarization anisotropy was

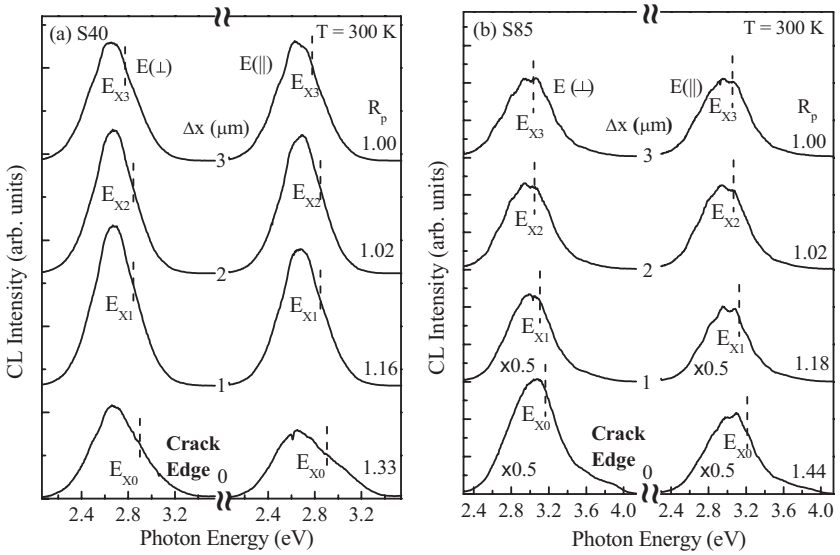

FIG. 2. CL spectra acquired locally with the e-beam focused to a spot at various distances Δx from the microcrack for samples S-40 and S-85 in (a) and (b), respectively. The intensities of some of the spectra have been scaled to more easily facilitate a comparison, as shown. The spectra were acquired with $T=300$ K, $I_b=200$ pA, and $E_b=15$ keV. The vertical dashed lines near the peaks of each spectrum indicate values of the calculated ground-state QD excitonic transition energy E_{xi} at the positions i (in units of μm) relative to the microcrack that were obtained from the model calculations. The intensity ratio R_p for each pair of spectra is indicated.

performed by averaging the intensities represented in the pixels from the polarized CL images of Fig. 1. This method minimizes the variations associated with local strain variations and sample surface degradation during measurements due to the averaging of small spatial intensity fluctuations. The results are presented in Figs. 3(a) and 3(b) for samples S85 and S40, respectively, for temperatures of 300 and 91 K. The polarization anisotropy ratio $R_p=I_\perp/I_\parallel$ exhibits a maximum of ~1.5 and ~1.3 for samples S85 and S40, respectively, near the microcrack and decreases to a value of ~1 over a range of ~3–4 μm from the microcrack. It is interesting to observe that the effect of lowering the temperature from 300 to 91 K is to increase the distance from the crack at which R_p is close to its relative maximum for both samples. The broadening of the distance from the microcrack at which $R_p>1$ apparently indicates an enhancement in the range of uniaxial stress at low temperatures due to a further contraction of the GaN/AlN film relative to Si. For distances greater than ~3 μm from the microcrack at both high and low temperatures R_p approaches unity, indicating the presence of biaxial stress in both samples. The measured range over which we observe a transition from uniaxial stress to biaxial stress is also consistent with a similar range ($\Delta x \approx 3$ μm) over which the measured radiative lifetime changes in the S40 and S85 samples.[11] An increase in the carrier lifetime by ~50% was measured for regions near the microcracks relative to that for regions greater than ~3 μm from the cracks.[11] This spatial variation of lifetime was attributed to an ~50% smaller oscillator strength between electrons and holes for GaN/AlN QDs subject to a uniaxial tensile stress relative to the oscillator strength for QDs subject to a biaxial tensile stress.[11]

V. THEORETICAL MODELING OF THE POLARIZATION ANISOTROPY IN GaN/AlN QUANTUM DOTS

A. Calculation of the polarization-dependent momentum matrix elements

The calculation of the in-plane polarization anisotropy was carried out with a multiband $\boldsymbol{k}\cdot\boldsymbol{p}$ method for calculating electron and hole wave functions, $\psi_e(\boldsymbol{r})$ and $\psi_h(\boldsymbol{r})$, respectively. In order to test the various hypotheses involving uniaxial stress and the resultant partial linear polarization near a microcrack, we first needed to develop a detailed model regarding the structural geometry of the QDs for both the S40 and S85 samples. The isolated QD in our model is a single GaN truncated hexagonal pyramid situated on a 1-nm-thick wetting layer (WL) and embedded in an AlN matrix. The average QD heights and volumes are known from previous TEM investigations of these samples and are 5.0 nm and 370 nm^3 and 3.7 nm and 230 nm^3, respectively, for samples S-40 and S-85.[5,27] In our model, we have constrained these heights and volumes to be constants in our calculations while allowing the area of both the top and bottom hexagonal faces of the truncated pyramid to independently vary. Essentially, the aspect ratio of the pyramid was varied in order to enable fits of the calculated *e-h* transition energies E_x to the experimental values determined from the CL spectra of Fig. 2 for both samples. By using these assumptions, the QD pyramidal aspect ratio and the AlN strain components were changed in a series of simulations in order to determine the resulting uniaxial stress near the crack and biaxial stress far from the crack in the AlN barrier for both samples. The height-to-diameter aspect ratios from the fits were 0.33 and 0.28 for the structures of S40 and S85, respectively, which were consistent with a range of 0.2–0.3 observed in previous TEM studies.[5,27,28]

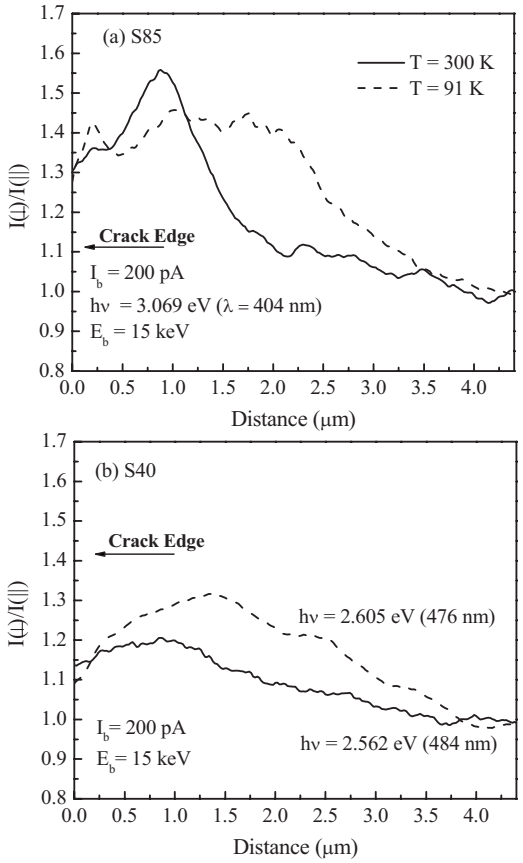

FIG. 3. CL line scans of the anisotropy ratio $I_\perp/I_\parallel$ vs distance from a microcrack for samples S85 and S40 in (a) and (b), respectively. The CL imaging conditions are indicated in each panel. Separate line scans were obtained for temperatures of 91 and 300 K.

From the results of the fits for the case of biaxial stress, the average electric fields in the QDs, along a line passing through the center of the dot and parallel to [0001], are 3.1 and 2.8 MV/cm for the structures of S-40 and S-85, respectively. For uniaxial stress near the microcrack, the average fields increase to 3.4 and 3.3 MV/cm for QDs in the S-40 and S-85 structures, respectively. Due to these large fields, the electron wave function is localized near the top of the QD, while the hole wave function is localized near the WL under the QD.[6,11,22,29] The larger QD (structure of sample S-40) exhibits a reduced energy separation between single particle electron and hole levels that is expected to lead to the observed spectral redshift of ~500 meV relative to emission from sample S-85.[11] The calculated excitonic transition energies E_x as a function of distance for the microcracks are shown with the vertical dashed lines for both samples in Fig. 2. The reduction in E_x for sample S-40 is therefore mainly due to the larger distance over which the electric field acts on electrons and holes.

The oscillator strength ratio is based on calculating the momentum matrix elements, $M_\perp$ and $M_\parallel$, in the dipole approximation. The momentum matrix elements are given by $M_{\perp,\parallel}=\langle\psi_e|\hat{e}_{\perp,\parallel}\cdot(\hbar/i)\vec{\nabla}|\psi_h\rangle$, where $\hat{e}_\perp$ and $\hat{e}_\parallel$ are unit vectors representing the directions of polarization of the emitted light which are perpendicular and parallel, respectively, to the [11−20] microcrack orientation. The Bloch part of the electron wave function $|\psi_e\rangle$ is represented by two basis s-like states $|S\uparrow\rangle$ and $|S\downarrow\rangle$ and denoted by $|j\rangle$. The Bloch part of the hole wavefunctions $|\psi_h\rangle$ can be represented by the six basis p-like functions $|i\rangle$ in the following representation: $|x\uparrow\rangle$, $|y\uparrow\rangle$, $|z\uparrow\rangle$, $|x\downarrow\rangle$, $|y\downarrow\rangle$, and $|z\downarrow\rangle$, where coordinates x, y, and z refer to the [1−100], [11−20], and [0001] crystallographic directions. The polarization dependent momentum matrix element can be further expressed as

$$M_{\perp,\parallel}=\left\langle\sum_{j=1}^{2}F_{e,j}^{*}(\vec{r})\langle j|\;\middle|\;\hat{e}_{\perp,\parallel}\cdot\frac{\hbar}{i}\vec{\nabla}\;\middle|\;\sum_{i=1}^{6}F_{h,i}(\vec{r})|i\rangle\right\rangle$$
$$\cong\sum_{j=1}^{2}\sum_{i=1}^{6}\int d^3rF_{e,j}^{*}(\vec{r})F_{h,i}(\vec{r})\langle j|\hat{e}_{\perp,\parallel}\cdot\frac{\hbar}{i}\vec{\nabla}|i\rangle, \quad (1)$$

where $F_{h,i}(\vec{r})$ are the six hole envelope functions that are obtained from the 3D 6×6 $\boldsymbol{k}\cdot\boldsymbol{p}$ method and $F_{e,j}(\vec{r})$ are the two electron envelope functions that are obtained from the 3D single effective mass calculation. We employ the standard approximation in the integration of Eq. (1), in which the envelope functions slowly vary in space in comparison to that of the Bloch functions. The evaluation of the integrals in Eq. (1) further requires calculating integrals over the unit cells involving the Bloch s- and p-like wave functions for the conduction and valence states possessing parallel spins as

$$\langle j|\frac{\partial}{\partial x_k}|i\rangle=\delta_{i,k}\sqrt{\frac{m_OE_P}{2\hbar^2}}, \quad (2)$$

where $\delta_{i,k}$ is the Kronecker delta (i,k vary from 1 to 3) and E_p is the Kane energy, which we take as 20 eV.[30] When choosing a certain polarization direction along the orthogonal Cartesian directions, i.e., $\hat{e}=\hat{x},\hat{y},\hat{z}$, only a Bloch function of the same character with its corresponding envelope function for each spin takes part in the calculation. For example, when $\hat{e}=\hat{x}$ (i.e., $\hat{e}_\perp$ in the experimental geometry), the matrix element $M_\perp$ only contains Bloch hole basis p_x states $\{|x\uparrow\rangle,|x\downarrow\rangle\}$. Thus, the polarization direction selects the envelope functions $F_{h,i}(\vec{r})$ that will be in the calculation for M. The polarization anisotropy ratio R_p is then calculated from Eq. (1) as

$$R_p=\frac{I_\perp}{I_\parallel}=\left|\frac{M_\perp}{M_\parallel}\right|^2, \quad (3)$$

which we will compare to the experimental results as a function of the stress components σ_{xx} and σ_{yy} and distance from the microcracks.

B. Modeling of the stress and strain tensors in the quantum dot

The strain-induced effects of the microcracks are modeled through stress in the AlN barrier, which is biaxial ($\sigma_{xx}=\sigma_{yy}$) for regions far from the crack and approximately uniaxial ($\sigma_{xx}=0$) for regions near the crack. We assume that σ_{xx} linearly varies for distances Δx from the microcrack that are in the range $0\leqslant\Delta x\leqslant3$ μm.[11] The stress in the underlying AlN barrier creates a strain, which is calculated accord-

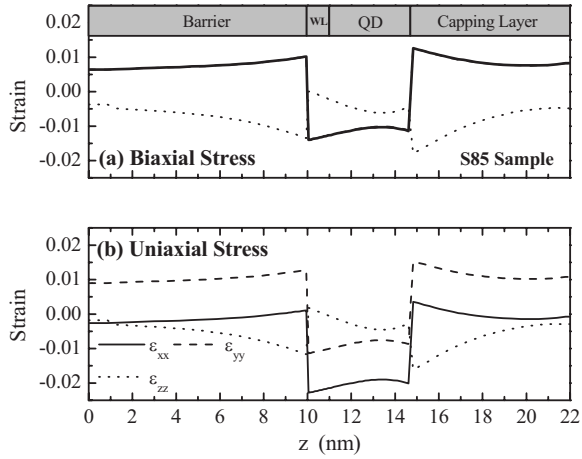

FIG. 4. The diagonal strain components ε_{ii} vs z along a line through the center of the QD and parallel to [0001] for the structure of S85. The results for the minimization of the elastic energy are shown for the cases of biaxial tensile stress and uniaxial tensile stress in (a) and (b), respectively. The positions of the AlN barrier, GaN wetting layer, GaN QD, and AlN capping layer are indicated in the gray heading.

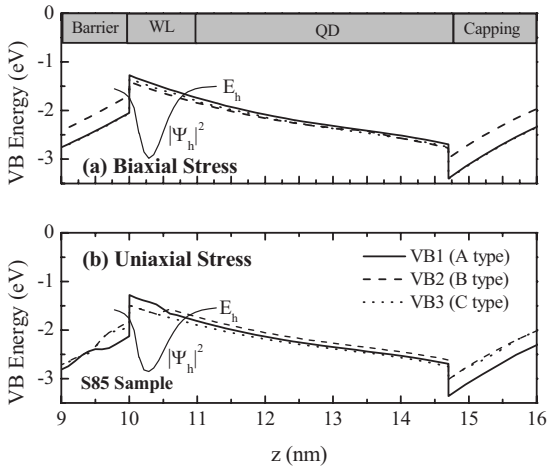

FIG. 5. The calculated valence band edge profiles along a line through the center of the QD and parallel to [0001] for the structure of S85. The calculations of the three highest valence band edges, denoted as A, B, and C, are shown for the cases of biaxial tensile stress in (a) and uniaxial tensile stress in (b). The results are obtained by diagonalization of the 6×6 Pikus–Bir strain Hamiltonian at each point using the six strain components ε_{ij} obtained from the minimization of the elastic energy. The probability density for the ground-state hole wavefunction $|\psi_h(\vec{r})|^2$ integrated over the x-y plane is also shown interposed on the valence band diagrams in (a) and (b), illustrating the strong localization in the WL.

ing to the elastic compliance tensor and provides boundary conditions for the input to the 3D strain minimization procedure for the hexagonal GaN QD. For an in-plane biaxial tensile stress ($\sigma_{xx}=\sigma_{yy}=S_b$, $\sigma_{zz}=0$) on an AlN film, the strain components are given by $\varepsilon_{xx}=\varepsilon_{yy}=(C_{11}+C_{12}-2C_{13}^2/C_{33})^{-1}S_b$ and $\varepsilon_{zz}=-(2C_{13}/C_{33})\varepsilon_{xx}$,[31] where the elastic constants are given by Wright as $C_{11}=3960$, $C_{12}=1370$, $C_{13}=1080$, and $C_{33}=3730$ kbar.[23,32] Similarly, near the microcrack, an in-plane uniaxial stress ($\sigma_{yy}=S_u$, $\sigma_{xx}=\sigma_{zz}=0$) is expected, in which $S_u\approx S_b$, where S_b and S_u represent the magnitude of the biaxial and uniaxial stresses, respectively, in the AlN film. By performing a series of iterations that involve calculating the strain tensor components and QD e-h transition energies E_x for the complete truncated pyramidal model system as a function of biaxial and uniaxial stress in the AlN barriers, we obtained biaxial tensile stress values S_b of ~30 and ~15 kbar at room temperature for samples S-85 and S-40, respectively. The resulting calculated values of E_x are shown in Fig. 2 by the four vertical dotted lines for each sample, which indicate distances of 0, 1, 2, and 3 μm from the microcrack. The magnitude of the stress values are consistent with previous results obtained in the literature for III-nitride films grown on Si.[33] As expected, a reduced tensile stress in the AlN barrier is found in sample S-40 relative to S-85 as a result of the reduced average Ga composition in S-40 relative to that for S-85.

The procedure for minimization of the elastic energy while subject to the applied thermal tensile stresses yielded strain values in the GaN QD that are still compressive. Figure 4 shows the diagonal strain components ε_{ii} for both biaxial and uniaxial stresses as a function of z along the [0001] growth direction through a point which passes through the center of the QD for the structure of S-85. In the case of biaxial tensile stress with $\sigma_{xx}=\sigma_{yy}=30$ kbar in the barrier, the strain components ε_{xx} and ε_{yy} in the QD are calculated to be equal and compressive (negative). For a uniaxial tensile stress ($\sigma_{yy}=30$ kbar and $\sigma_{xx}=\sigma_{zz}=0$), $|\varepsilon_{xx}|>|\varepsilon_{yy}|$ in the QD, but ε_{xx} and ε_{yy} are still compressive with ε_{xx} being more compressive, as expected from the applied uniaxial stress in the barrier. Of critical importance is the behavior of the diagonal ε_{ii} components in the wetting layer for varying stress tensors, as this will be shown to affect the relative admixture of the p_x, p_y, and p_z characters of the hole wave functions and subsequently the calculation of the polarization anisotropy. Similar results were obtained for the structure of sample S-40 and are therefore not shown.

C. Determination of the strain-split band edges of the quantum dot and wetting layer

After completion of the 3D strain minimization procedure, the conduction and valence band edges were determined in the usual manner from diagonalization of the Pikus–Bir strain Hamiltonian for all points in the AlN/GaN pyramidal QD model grid.[34] The band edge profiles for the structure of S85 are shown for the cases of biaxial and uniaxial stress in Figs. 5(a) and 5(b), respectively, as one-dimensional line scans of the valence band edge energies vs distance z along lines passing through the QD center in the [0001] direction. The three upper most valence bands at $k=0$ are labeled as A, B, and C, which is a common notation for such bands in wurtzite crystals. The probability density for the ground-state hole wave function $|\psi_h(\vec{r})|^2$ integrated over the x-y plane is shown in Figs. 5(a) and 5(b), illustrating again the strong localization in the WL. We observe that the hole is localized near the center of the wetting layer beneath the center of the pyramidal QD for the cases of both uniaxial and biaxial stress. We have also calculated the relative

TABLE I. The relative weights, $f_{ij}=|\langle i|j\rangle|^2$, of the Bloch characters $|x\rangle$, $|y\rangle$, and $|z\rangle$ in each of the bands A, B, and C at a point near the center of the hole localization in the wetting layer.

	Biaxial stress			Uniaxial stress		
	$\|\langle i\|A\rangle\|^2$	$\|\langle i\|B\rangle\|^2$	$\|\langle i\|C\rangle\|^2$	$\|\langle i\|A\rangle\|^2$	$\|\langle i\|B\rangle\|^2$	$\|\langle i\|C\rangle\|^2$
$\langle x\|$	0.5	0.5	0	0	1.0	0
$\langle y\|$	0.5	0.5	0	1.0	0	0
$\langle z\|$	0	0	1.0	0	0	1.0

p-orbital admixtures of the Bloch states $|x\rangle$,$|y\rangle$, and $|z\rangle$ in each of the bands A, B, and C at the point near the center of the hole localization (i.e., where its probability density is a maximum). The results are shown in Table I and presented as $f_{ij}=|\langle i|j\rangle|^2$, where $i=x,y,z$ and $j=A,B,C$ for the cases of pure uniaxial stress and biaxial stress. The calculation for f_{ij} takes into account sums over both spin projections $|\uparrow\rangle$ and $|\downarrow\rangle$. As expected for biaxial stress, equal admixtures of $|x\rangle$ and $|y\rangle$ are found in the A and B band edges, while the C band contains only the $|z\rangle$ orbital (i.e., p_z character). For the case of uniaxial stress, the particular stress conditions yield $\varepsilon_{yy}=-0.0107$, $\varepsilon_{xx}/\varepsilon_{yy}\approx 2$, and $1.8\times 10^{-4}\geq\varepsilon_{zz}\geq -4\times 10^{-4}$ within the WL (i.e., for $10\leq z\leq 11$ nm) of the QD. The resulting diagonalization of the strain Hamiltonian yields A, B, and C bands that exhibit nearly unmixed $|x\rangle$, $|y\rangle$, and $|z\rangle$ p characters, as shown in Table I. For the case of uniaxial stress in Fig. 5(b), a reversal in the ordering of the A and B bands is observed near the middle of the WL ($z\approx 10.6$ nm) and correlates with a decrease of ε_{zz}, owing to the sensitive contributions of the products of ε_{ii} and the strain deformation potentials, D_1–D_6 in the strain Hamiltonian. The changes in the character and ordering of the band edges are expected to result in corresponding changes in the character of the confined hole wave functions, which in turn affect the calculated polzarization anisotropy, $I_\perp/I_\parallel$. In the next section, we will attempt to correlate the various Bloch characters of the hole wave functions with the character weights f_{ij} of the band edges in attempt to develop a model for the polarization anisotropy.

D. Comparison of theory to experiment

From the 3D calculations of $\psi_e(\boldsymbol{r})$ and $\psi_h(\boldsymbol{r})$, the momentum matrix elements contained in Eq. (1) were determined for light possessing the two in-plane orthogonal polarizations $\boldsymbol{E}_\parallel$ and $\boldsymbol{E}_\perp$ relative to the [11−20]-oriented microcracks. The polarization anisotropy ratio R_p for light polarized along the [11−20] and [1−100] directions was calculated for various distances from the crack, as shown in Fig. 6. A nearly linear decrease in R_p is observed over distances from 0 to 3 μm from the edge of the crack for both samples, as the stress tensor gradually changes from pure uniaxial stress to biaxial stress. When the QD is subject to a pure biaxial stress ($\sigma_{xx}=\sigma_{yy}$), the calculations yield $R_p\approx 1$, as expected from symmetry considerations. The calculated ratio R_p for the S40 structure is smaller than that for the S85 due to a reduced value of S_b for the S40 sample (i.e., ~15 vs 30 kbar), as also

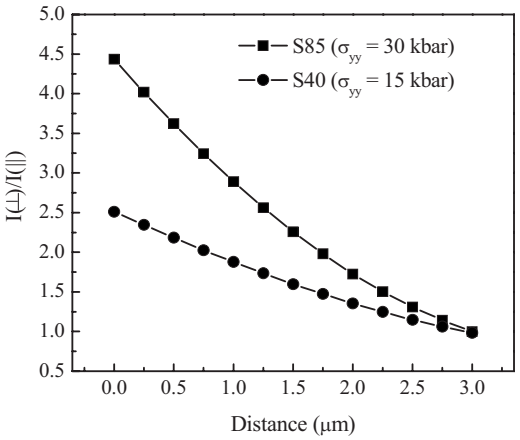

FIG. 6. The calculated anisotropy ratio $I_\perp/I_\parallel$ vs distance from a microcrack for structures S40 and S85.

observed for the experimental results of both samples in Figs. 2 and 3. The results displayed in Fig. 6 qualitatively agree with the experimental results in Fig. 3, which show R_p vs distance for both samples. The maximum experimental values for R_p, which are ~1.5 and ~1.3 for samples S85 and S40, are less than the calculated values of 4.5 and 2.5, respectively, for room temperature. We attribute a smaller experimental value of R_p as due in part to (i) the depolarization effects of the mirror, which will limit the maximum measured value of R_p to ~3.7 (see Sec. II), and (ii) deviations from pure uniaxial stress (i.e., $\sigma_{yy}=S_u$ and $\sigma_{xx}=\sigma_{zz}=0$) caused by shear, peeling, and residual stress components near the crack. The latter stress components were previously studied in GaAs films on Si(001) with polarized CL, which showed that a residual σ_{xx} component, having a magnitude of ~25% of σ_{yy}, is present at the edge of some films.[35]

The polarization dependence of the momentum matrix elements can be better understood by examining strain-induced changes in the hole wave functions that are obtained from the $\boldsymbol{k}\cdot\boldsymbol{p}$ calculations. Isosurfaces of the ground-state hole wave function of the QD [with $|\psi_h(\vec{r})|^2=0.1|\psi_{\max}|^2$, where $|\psi_{\max}|^2$ is the maximum probability density of the hole state] for the S85 structure at distances of 0, 1, 2, and 3 μm from the microcrack are presented in Fig. 7. Similar results were obtained for the structure of S40. A gradual change in shape and direction of elongation of the isosurface are observed in the sequence from 0 to 3 μm. Furthermore, the envelope functions $F_{h,i}(\vec{r})$ will vary with strain, thereby altering the relative character of the Bloch components that comprise the ground-state hole wave function. It is possible to observe the position dependent character of the wave function by projecting the three Bloch states with like spin, $|x\rangle$, $|y\rangle$, and $|z\rangle$, onto the hole wave function by calculating $f_{WFi}=|\langle i|\psi_h\rangle|^2$, where $i=x$, y, and z, as shown in Fig. 8. The relative p-orbital character of the Bloch states f_{WFi} dramatically changes in transitioning from 0 to 3 μm, i.e., from regions of uniaxial to biaxial stress. The weight of the character f_{WFy} changes from 0.91 to 0.44, while f_{WFx} changes from 0.0409 to 0.439 along this path, as shown in Fig. 8. These weights further correlate with the weights of the band edge p-characters f_{ij} that are shown in Table I. The hole band edge

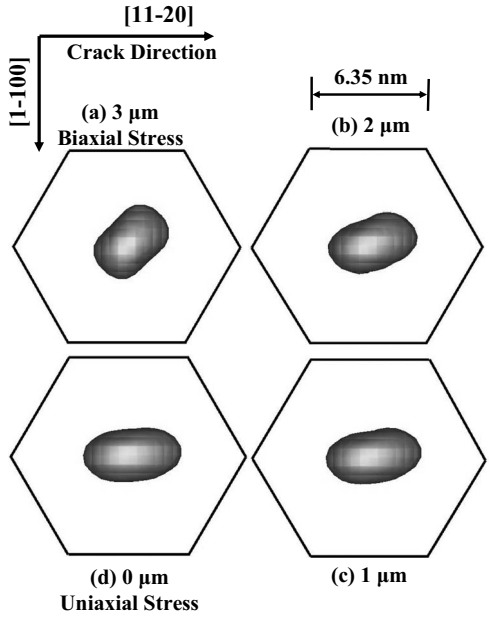

FIG. 7. Isosurfaces of the ground-state hole wave functions for the structure of S85. Surfaces of constant probability density, $|\psi_h(\vec{r})|^2=0.1|\psi_{\max}|^2$, are plotted for distances of 0, 1, 2, and 3 μm from the microcrack. Distances of 0 and 3 μm correspond to the conditions of pure uniaxial and biaxial tensile stress, respectively. The hexagonal base of the pyramidal GaN QD is shown for each isosurface. The apparent variations in shade on the isosurfaces are due to a simulated reflection of light rays impinging on the surface from above.

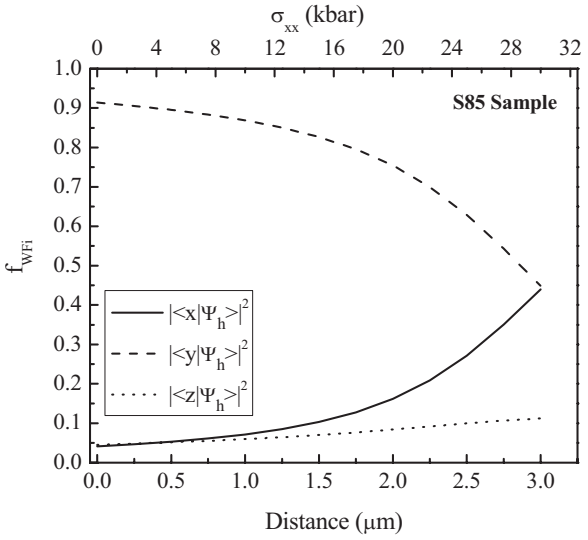

FIG. 8. The weight of the $|x\rangle$, $|y\rangle$, and $|z\rangle$ characters of the hole wave function f_{WFi} vs distance from the microcrack for the structure of S85. As discussed in the text, we use the defintion $f_{WFi}=|\langle i|\psi_h\rangle|^2$, where $i=x$, y, and z. The value of the corresponding stress component σ_{xx} is shown on the top axis in transitioning from uniaxial to biaxial stress for distances ranging from 0 to 3 μm from the microcrack.

A possessing lowest energy in the uniaxial case exhibits a weight $f_{yA}=1.0$ for the $|y\rangle$ character, which is consistent with the aforementioned weight (0.91) of the ground state hole wave function. Likewise, the mixed characters of hole wave function at a distance of 3 μm, as indicated by $f_{WFx}\approx f_{WFy}$, also reflect the mixed characters of the A and B band edges, $f_{xA}=f_{xB}$, for the case of biaxial stress.

The vivid changes in direction of elongation of the isosurfaces are also consistent with the large changes in the calculated R_p. For the case of uniaxial stress in Fig. 7(d) for the structure S85, the isosurface, as determined by the spatial distribution of the envelope functions $F_{h,i}(\vec{r})$ that comprise the hole state, is nearly entirely elongated along the $[11-20]$ crack direction and reflects the primarily $|y\rangle$ character of the wavefunction. Similarly, the nearly equal admixtures of $|x\rangle$ and $|y\rangle$ characters for biaxial stress yield nearly equal contributions of their envelope functions whose elongations are in orthogonal directions. The result is an elongation of the isosurface along a direction that is oriented $\sim 45°$ with respect to the $[11-20]$ crack direction for the case of biaxial stress, as shown in Fig. 7(a). These results illustrate a strong correlation between the shape and elongation direction of the hole isosurface, the relative p characters of the hole wave function, and the measured and calculated polarization anisotropy ratios R_p.

VI. CONCLUSIONS

Cathodoluminescence spectroscopy and imaging measurements of the ground-state excitonic transition of vertically stacked GaN/AlN QDs exhibited an in-plane linear polarization anisotropy, which is largest in close proximity to microcracks. The microcracks serve as an excellent stressor through which the strain tensor of the GaN/AlN QDs can be modified reproducibly for studies of strain-induced changes in the optical and electronic properties using a spatially resolved probe, such as with CL. While the presence of thermal stress-induced microcracks is clearly undesirable when attempting to obtain high-quality thin film growth of III-nitride films and QDs on Si substrates, the presence of microcracks, however, enables a study of potentially interesting strain-induced changes in optical polarization, as we have demonstrated. These results suggest that proper control of thermal strain for the growth of GaN/AlN QDs on patterned substrates could also be used to manipulate the polarization anisotropy in excitonic complexes for applications in quantum information processing, in which the essential element is an optical source that emits a train of single photons.[36,37]

Changes in the optical polarization properties are attributed to stress-dependent variations in the p_x and p_y characters of the band edges and the ground-state hole wave function. A minimization of the elastic energy for modeled GaN/AlN QD structures with applied uniaxial and biaxial stresses for the determination of $\varepsilon_{ij}(\boldsymbol{r})$ and 3D 6×6 $\boldsymbol{k}\cdot\boldsymbol{p}$ calculations of the QD hole wave functions and eigenstates were performed to examine the influence of biaxial and uniaxial tensile stresses on the polarization-dependent momentum matrix elements in varying proximity to the microcracks. The model reveals that a change from biaxial to uniaxial stress alters the admixture of p_x and p_y characters of the band edges and ground state hole wave function, changes the shape and direction of elongation of the hole isosurfaces, and accounts well for the subsequent anisotropy in the polarization depen-

dent optical transitions and its spatial variation in the vicinity of the microcracks.

ACKNOWLEDGMENTS

We would like to thank S. Birner and M. Povolotskyi for consultations and modifications of their NEXTNANO³ quantum nanostructure simulation code. This work was supported in part by the Israel Science Foundation (ISF Grant No. 8/02-1).

[1] S. Tanaka, H. Hirayama, Y. Aoyagi, Y. Narukawa, Y. Kawakami, and S. Fujita, Appl. Phys. Lett. **71**, 1299 (1997).
[2] B. Damilano, N. Grandjean, F. Semond, J. Massies, and M. Leroux, Appl. Phys. Lett. **75**, 962 (1999).
[3] B. Damilano, N. Grandjean, J. Massies and F. Semond, Appl. Surf. Sci. **164**, 241 (2000).
[4] F. Widmann, J. Simon, B. Daudin, G. Feuillet, J. L. Rouviere, N. T. Pelekanos, and G. Fishman, Phys. Rev. B **58**, R15989 (1998).
[5] S. Kalliakos, T. Bretagnon, P. Lefebvre, T. Taliercio, B. Gil, N. Grandjean, B. Damilano, A. Dussaigne, and J. Massies, J. Appl. Phys. **96**, 180 (2004).
[6] A. D. Andreev and E. P. O'Reilly, Phys. Rev. B **62**, 15851 (2000).
[7] T. Bretagnon, P. Lefebvre, P. Valvin, R. Bardoux, T. Guillet, T. Taliercio, B. Gil, N. Grandjean, F. Semond, B. Damilano, A. Dussaigne, and J. Massies, Phys. Rev. B **73**, 113304 (2006).
[8] L. Liu and J. H. Edgar, Mater. Sci. Eng., R. **37**, 61 (2002).
[9] A. Dadgar, A. Strittmatter, J. Bläsing, M. Poschenrieder, O. Contreras, P. Veit, T. Riemann, F. Bertram, A. Reiher, A. Krtschil, A. Diez1, T. Hempel, T. Finger, A. Kasic, M. Schubert, D. Bimberg, F. A. Ponce, J. Christen, and A. Krost, Phys. Status Solidi C **0**, 1583 (2003).
[10] D. Rudloff, T. Riemann, J. Christen, Q. K. K. Liu, A. Kaschner, A. Hoffmann, Ch. Thomsen, K. Vogeler, M. Diesselberg, S. Einfeldt, and D. Hommel, Appl. Phys. Lett. **82**, 367 (2003).
[11] G. Sarusi, O. Moshe, S. Khatsevich, D. H. Rich, and B. Damilano, Phys. Rev. B **75**, 075306 (2007).
[12] H. Kawanishi, E. Niikura, M. Yamamoto, and S. Takeda, Appl. Phys. Lett. **89**, 251107 (2006).
[13] J. Shakya, K. Knabe, K. H. Kim, J. Li, J. Y. Lin, and H. X. Jiang, Appl. Phys. Lett. **86**, 091107 (2005).
[14] B. Gil and O. Briot, Phys. Rev. B **55**, 2530 (1997).
[15] K. Domen, K. Horino, A. Kuramata, and T. Tanahashi, Appl. Phys. Lett. **71**, 1996 (1997).
[16] B. Rau, P. Waltereit, O. Brandt, M. Ramsteiner, K. H. Ploog, J. Puls, and F. Henneberger, Appl. Phys. Lett. **77**, 3343 (2000).
[17] M. Winkelnkemper, R. Seguin, S. Rodt, A. Schliwa, L. Reißmann, A. Strittmatter, A. Hoffmann, and D. Bimberg, J. Appl. Phys. **101**, 113708 (2007).
[18] B. Daudin, F. Widmann, G. Feuillet, Y. Samson, M. Arlery, and J. L. Rouviere, Phys. Rev. B **56**, R7069 (1997).
[19] M. Miyamura, K. Tachibana, and Y. Arakawa, Appl. Phys. Lett. **80**, 3937 (2002).
[20] D. H. Rich, A. Ksendzov, R. W. Terhune, F. J. Grunthaner, B. A. Wilson, H. Shen, M. Dutta, S. M. Vernon, and T. M. Dixon, Phys. Rev. B **43**, 6836 (1991).
[21] K. H. Lee, J. H. Na, R. A. Taylor, S. N. Yi, S. Birner, Y. S. Park, C. M. Park, and T. W. Kang, Appl. Phys. Lett. **89**, 023103 (2006).
[22] V. A. Fonoberov and A. A. Balandin, J. Appl. Phys. **94**, 7178 (2003); J. Vac. Sci. Technol. B **22**, 2190 (2004).
[23] I. Vurgaftman and J. R. Meyer, J. Appl. Phys. **94**, 3675 (2003); I. Vurgaftman, J. R. Meyer, and L. R. Ram-Mohan, J. Appl. Phys. **89**, 5815 (2001).
[24] O. Ambacher, J. Majewski, C. Miskys, A. Link, M. Hermann, M. Eickhoff, M. Stutzmann, F. Bernardini, V. Fiorentini, V. Tilak, B. Schaff, and L. F. Eastman, J. Phys.: Condens. Matter **14**, 3399 (2002).
[25] D. P. Williams, A. D. Andreev, E. P. O'Reilly, and D. A. Faux, Phys. Rev. B **72**, 235318 (2005); D. P. Williams, A. D. Andreev, and E. P. O'Reilly, *ibid.* **73**, 241301(R) (2006).
[26] P. Bigenwald, P. Lefebvre, T. Bretagnon, and B. Gil, Phys. Status Solidi B **216**, 371 (1999).
[27] G. Salviati, F. Rossi, N. Armani, V. Grillo, O. Martinez, A. Vinattieri, B. Damilano, A. Matsuse, and N. Grandjean, J. Phys.: Condens. Matter **16**, S115 (2004).
[28] The diameter of the pyramidal base is defined as the maximum length of the hexagon along the $[11-20]$ direction (i.e., the maximal diameter of the hexagon). We also note that from the fits the areas for the top and bottom hexagonal faces are $A_{top}=20$ nm^2 and $A_{bottom}=146$ nm^2 for S40 and $A_{top}=31$ nm^2 and $A_{bottom}=104$ nm^2 for S85.
[29] S. L. Chuang and C. S. Chang, Semicond. Sci. Technol. **12**, 252 (1997).
[30] S. Shokhovets, G. Gobsch, and O. Ambacher, Appl. Phys. Lett. **86**, 161908 (2005).
[31] M. Born and K. Huang, *Dynamical Theory of Crystal Lattices* (Oxford University Press, London, 1968).
[32] F. Wright, J. Appl. Phys. **82**, 2833 (1997).
[33] G. Sarusi, O. Moshe, S. Khatsevich, D. H. Rich, J. Salzman, B. Meyler, M. Shandalov, and Y. Golan, J. Electron. Mater. **35**, L15 (2006).
[34] E. Berkowicz, D. Gershoni, G. Bahir, E. Lakin, D. Shilo, E. Zolotoyabko, A. C. Abare, S. P. Denbaars, and L. A. Coldren, Phys. Rev. B **61**, 10994 (2000).
[35] Y. Tang, D. H. Rich, E. H. Lingunis, and N. M. Haegel, J. Appl. Phys. **76**, 3032 (1994).
[36] G. Brassard, N. Lütkenhaus, T. Mor, and B. C. Sanders, Phys. Rev. Lett. **85**, 1330 (2000).
[37] S. De Rinaldis, I. D'Amico, E. Biolatti, R. Rinaldi, R. Cingolani, and F. Rossi, Phys. Rev. B **65**, 081309(R) (2002).